Bifunctional Catalysts

DOI: 10.1002/anie.201402710

Mn_xO_y/NC and Co_xO_y/NC Nanoparticles Embedded in a Nitrogen-Doped Carbon Matrix for High-Performance Bifunctional Oxygen Electrodes**

Justus Masa, Wei Xia, Ilya Sinev, Anqi Zhao, Zhenyu Sun, Stefanie Grützke, Philipp Weide, Martin Muhler, and Wolfgang Schuhmann**

Abstract: *Reversible interconversion of water into H_2 and O_2, and the recombination of H_2 and O_2 to H_2O thereby harnessing the energy of the reaction provides a completely green cycle for sustainable energy conversion and storage. The realization of this goal is however hampered by the lack of efficient catalysts for water splitting and oxygen reduction. We report exceptionally active bifunctional catalysts for oxygen electrodes comprising Mn_3O_4 and Co_3O_4 nanoparticles embedded in nitrogen-doped carbon, obtained by selective pyrolysis and subsequent mild calcination of manganese and cobalt N_4 macrocyclic complexes. Intimate interaction was observed between the metals and nitrogen suggesting residual $M–N_x$ coordination in the catalysts. The catalysts afford remarkably lower reversible overpotentials in KOH (0.1M) than those for RuO_2, IrO_2, Pt, NiO, Mn_3O_4, and Co_3O_4, thus placing them among the best non-precious-metal catalysts for reversible oxygen electrodes reported to date.*

The theoretically high energy density of metal–air batteries makes them very desirable for future energy conversion and storage applications.[1–4] However, unlike conventional secondary batteries, their rechargeability still poses many scientific challenges, one of which being the development of efficient catalysts for the oxygen-reduction reaction (ORR) during the discharge process, and for the oxygen-evolution reaction (OER) during the recharge process.[3,4] Finding stable and efficient electrocatalysts which drive both reactions is difficult, because good catalysts for ORR often tend to be poor for OER and vice versa.[1,4,5] For example, platinum which is a very good catalyst for ORR is poor for OER, while ruthenium and iridium oxides which are very good for OER are poor for ORR.[6–8] Most bifunctional catalysts are prepared by combining good catalysts for ORR and OER to form a composite.[9] At present, the premium catalysts of choice for both reactions comprise platinum-group metals,[6,9] which is a drawback from the point of view of cost and availability.

Transition-metal oxides which have structural and compositional semblance to the active center of the oxygen evolving complex, such as spinels, show catalytic activity towards both OER and ORR.[10] The electrocatalytic potency of most transition-metal oxides is impaired by their poor electronic conductivity, which however, may be improved by doping the oxides with electron donors or by supporting them on conducting materials.[11]

Herein, we exploited the unique structural and functional properties of porphyrins and phthalocyanines as precursors to synthesize manganese-based oxide catalysts with exceptionally high dual activity in electrocatalyzing both ORR and OER. The synthesis involved two key steps. In the first step, the macrocyclic complex (MnN_4) was impregnated with nitrogen-doped carbon (NC) followed by pyrolysis of the MnN_4/NC composite at 650 °C for 2 h under He. This step was followed by mild calcination of the product in oxygen at 200 °C for 30 min. The resulting catalyst is hereafter denoted as Mn_xO_y/NC. During the synthesis, the macrocyclic structures degrade to form among others, spinel Mn_3O_4 nanoparticles, and $Mn–N_x$ moieties embedded in a NC matrix. The nitrogen-functionalized carbon groups in NC, particularly, pyridinic, graphitic, and pyrrolic groups act as complementary ORR catalysts in addition to conferring conductivity to the Mn_3O_4 nanoparticles, thereby furnishing the catalyst the unusual capability to catalyze both ORR and OER with outstanding efficiency.

We observed that catalysts prepared from different porphyrin ligands (Figure 1S in the Supporting Information) show similar structural and electrochemical properties. We therefore used *meso*-tetrakis(4-pyridyl)porphyrinate manganese(III) (Figure 1S) as the precursor for detailed structural and electrochemical investigation of Mn_xO_y/NC.

[*] Dr. J. Masa, Dr. Z. Sun, S. Grützke, Prof. Dr. W. Schuhmann
Analytische Chemie—Zentrum für Elektrochemie (CES)
Ruhr-Universität Bochum
NC04/788, 44780 Bochum (Germany)
E-mail: wolfgang.schuhmann@rub.de
Homepage: http://www.rub.de/elan
Dr. W. Xia, Dr. I. Sinev, A. Zhao, P. Weide, Prof. Dr. M. Muhler
Lehrstuhl für Technische Chemie
Ruhr-Universität Bochum
NBCF 04/690, 44801 Bochum (Germany)
E-mail: muhler@techem.rub.de

[**] Financial support from the DFG (Deutsche Forschungsgemeinschaft) in the framework of the Cluster of Excellence RESOLV (EXC 1069) and in the framework of Helmholtz-Energie-Allianz "Stationäre elektrochemische Speicher und Wandler" (HA-E-0002) is gratefully acknowledged. A.Z. is grateful to the China Scholarship Council for a Ph.D. Scholarship. We thank Dr. Dennis König of the Department of Mechanical Engineering, Institute for Materials, Ruhr-University Bochum for the TEM measurements and Sandra Schmidt for the SEM measurements. The XAFS measurements were performed at CLÆSS beamline at ALBA Synchrotron Light Facility with the collaboration of ALBA staff.

Supporting information for this article is available on the WWW under http://dx.doi.org/10.1002/anie.201402710.

Representative SEM micrographs of Mn_xO_y/NC with superimposed energy-dispersive X-ray spectroscopy (EDX) spectra are shown in Figure 2S. The SEM images reveal agglomerated nanoparticles surrounded by an amorphous shell. Figure 1a shows TEM images of Mn_xO_y/NC at different

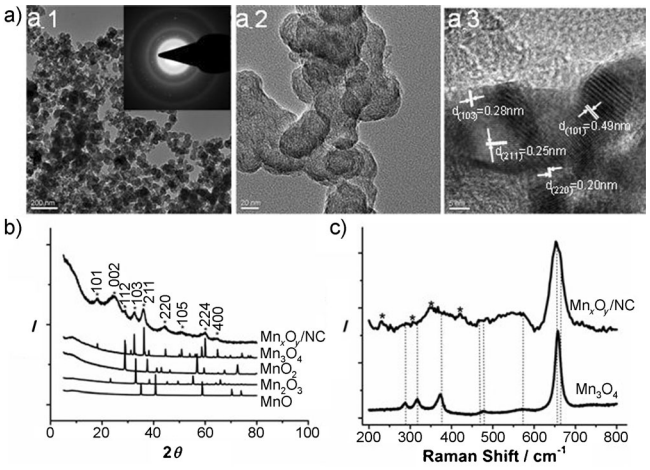

Figure 1. a) TEM images of Mn_xO_y/NC at different magnification scales, b) XRD patterns of Mn_xO_y/NC, and commercial MnO, Mn_2O_3, Mn_3O_4, and MnO_2, c) Raman spectra of Mn_xO_y/NC and Mn_3O_4 recorded at 661 nm and 10 mW laser power.

magnification scales in which nanoparticles can be seen that are either embedded in or surrounded by amorphous carbon. The selected-area electron diffraction (SAED) image (inset of Figure 1a-1) shows that the particles are polycrystalline. For the embedded particles, the surface of the amorphous carbon shell is highly porous (Figure 1a-2). The diffraction fringes in the high-resolution TEM image of Figure 1a-3 expose the different crystal planes of the particles. The observed lattice spacings of 0.49, 0.20, 0.28, and 0.25 nm correspond to the (101), (220), (103), and (211) crystal planes of tetragonal Mn_3O_4. This result was confirmed by the X-ray diffraction (XRD) results (Figure 1b). The diffraction peak at 24.57° originates from the (002) planes of carbon. The XRD pattern of Mn_xO_y/NC matches that of Mn_3O_4, space group $I4_1/$ and consistent with the JCPDS card file No. 24-0734 thus revealing the formation of crystalline Mn_3O_4 particles with a tetragonal hausmannite structure. The Raman spectrum of Mn_xO_y/NC (Figure 1c) was compared with that of Mn_3O_4. The reference sample, Mn_3O_4, shows the typical expected Raman bands with bands at 287.9, 317.3, 373.4, 657.6 cm^{-1}, and an additional weak band with a maximum at 570.5 cm^{-1}. A prominent band at 652.5 cm^{-1} assigned to A_{1g} symmetric stretching of the M–O bond of the MnO_6 octahedra unequivocally confirms the formation of Mn_3O_4 nanoparticles with a spinel structure.[12] The atypical shoulder discernible at 662.3 cm^{-1} is attributed to structural distortion resulting from intimate interaction of impurity atoms with the spinel structure. The low intensity bands at 229.5, 347.5, and 421.3 cm^{-1} are characteristic of Mn–N_4 and arise from stretching or deformation of out-of-plane Mn–N Raman modes,[13] confirmed by recording the Raman spectrum of manganese phthalocyanine under similar conditions (Figure 4S). These observations indicate that Mn–N bonds are apparently conserved in the final catalyst.

The ability of Mn_xO_y/NC to electrocatalyze both ORR and OER was investigated by hydrodynamic voltammetry in oxygen-saturated KOH (0.1M) and compared with commercial Mn_2O_3, Mn_3O_4, and MnO_2 (Figure 2a), and with IrO_2, RuO_2, and Pt/C (Figure 2b).

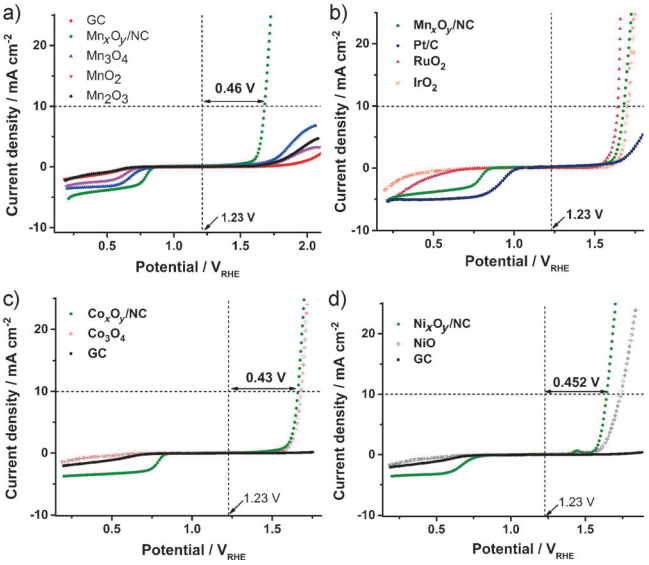

Figure 2. Linear-sweep voltammograms showing the electrocatalysis of oxygen reduction and water oxidation by a) Mn_xO_y/NC and commercial manganese oxides, b) Mn_xO_y/NC and Pt/C, IrO_2, and RuO_2, c) Co_xO_y/NC compared with Co_3O_4 and d) Ni_xO_y/NC compared with NiO, in oxygen saturated KOH (0.1 M) at a scan rate of 10 $mV s^{-1}$ and rotation of 1600 rpm. GC = Glassy carbon.

Mn_xO_y/NC clearly shows a higher oxygen-evolution current at all potentials compared to ordinary manganese oxides. The reduction of oxygen by Mn_xO_y/NC starts at a much lower overpotential and the reduction current is pronouncedly higher than that of any of the conventional oxides. We attribute the ability of Mn_xO_y/NC to catalyze both ORR and OER with much higher efficiency than ordinary manganese oxides to its unique structure and composition. The porous nitrogen-rich carbon shell surrounding the Mn_xO_y particles confers enhanced conductivity to the particles thus concertedly promoting their activity for both OER and ORR. Concomitantly, the ORR activity is further augmented by the nitrogen-functionalized carbon groups in NC.

Interestingly, the method also works very well when applied to synthesize corresponding cobalt, Co_xO_y/NC (Figure 2c) and nickel, Ni_xO_y/NC (Figure 2d) catalysts, which outperform Co_3O_4 and NiO, respectively, for both ORR and OER.

The overvoltage between ORR and OER translates into loss in efficiency and is therefore a very important parameter for evaluating the bifunctional electrocatalytic activity of a given catalyst (Table 1). The OER activity was computed as

Table 1: The bifunctional activity of various catalysts for ORR and OER.

Catalyst	E_{ORR}/V 1 mA cm^{-2}	E_{OER}/V 10 mA cm^{-2}	ΔE/V ($E_{ORR}-E_{OER}$)
RuO_2	0.54	1.64	1.10
IrO_2	0.38	1.70	1.32
Pt/C	0.96	1.90	0.94
Mn_xO_y/NC	0.81	1.68	0.87
Ni_xO_y/NC	0.71	1.64	0.93
NiO	0.32	1.74	1.42
Co_xO_y/NC	0.80	1.66	0.86
Co_3O_4	0.27	1.68	1.41

the potential at a current density of 10 mA cm^{-2}, which has been proposed as a figure-of-merit for the viability of a given catalyst in solar fuel synthesis.[14] The ORR activity of the catalysts was compared at the potential corresponding to a current density of 1 mA cm^{-2} during oxygen reduction. Strikingly, the low overvoltage between ORR and OER would translate into an energy saving of at least 80 mV, 70 mV, and 10 mV, respectively, if instead of Pt/C, the Co_xO_y/NC, Mn_xO_y/NC, and Ni_xO_y/NC bifunctional catalysts are used.

The chemical interaction of the various components of Mn_xO_y/NC and Co_xO_y/NC was probed by X-ray photoelectron spectroscopy (XPS). The Mn 2p signals (Figure 3a) have doublets at 641.4 eV (Mn $2p_{3/2}$) and 653.3 eV (Mn $2p_{1/2}$) corresponding to a spin-orbit splitting of 11.80 eV typical of Mn_3O_4.[15] The weak shoulder at 639.1 eV, untypical of manganese oxides, is ascribed to Mn–N_x moieties as confirmed by Raman spectroscopy. The Co 2p core-level spectrum (Figure 3b) is devoid of any shake-up peaks and the Co $2p_{1/2}$ and Co $2p_{3/2}$ bands are centered at 780.7 eV and 796.2 eV with a separation of 15.5 eV between them, typical of Co_3O_4 in very good agreement with well-characterized Co_3O_4.[16] The broad shoulder centered at 778.8 eV is uncharacteristic of cobalt oxides and oxyhydroxides, or of Co^0 whose signal is expected at (778.1 ± 0.02) eV.[16] The Co–N_4 core has been observed to be conserved during pyrolysis of cobalt-containing N_4-macrocyclic complexes at low temperatures (< 700 °C).[17,18] We therefore ascribe this shoulder to the presence of Co–N_x moieties in Co_xO_y/NC. The N 1s spectra of both Co_xO_y/NC and Mn_xO_y/NC were deconvoluted into three peaks. The co-existence of nitrogen-doped carbon in the catalysts complicates unambiguous assignment of the peaks. However, a literature survey indicates that the unusually sharp intensity of the low-binding-energy signals of the N 1s spectra of both Mn_xO_y/NC (Figure 3c) and Co_xO_y/NC (Figure 3d) cannot be exclusively due to the commonly encountered nitrogen-functionalized carbon groups, namely pyridinic, pyrrolic, and quaternary, expected at 398.6, 400.3, and (401.3 ± 0.3) eV, respectively,[19,20] indicating that a fraction of the metal centers apparently remain coordinated to nitrogen.

The O 1s region of Mn_xO_y/NC was deconvoluted into three different contributions at 530.8, 532.2, and 533.7 eV. The sharp peak at a binding energy of 530.8 eV is due to lattice oxygen (O^{2-}) of Mn_3O_4. The lower intensity peaks at 532.1 eV and 533.4 eV are due to oxygen-containing functional groups on the carbon surface.[20] The O 1s region of Co_xO_y/NC was also deconvoluted into three contributions at 531.0 eV and 532.2 eV assigned to coordinatively unsaturated oxygen species and surface hydroxylation respectively, and at 533.7 eV assigned to oxygen groups on the carbon surface (Figure 3f).[21]

The X-ray near edge structure (XANES) of Co_xO_y/NC shows the spectral features typical of both metallic cobalt and CoO. The pre-edge region, formed by 1s→3d electron transition is represented with two peaks (marked "a" and "a*" in Figure 4a) at 7709 eV and 7711 eV. The 7709 eV peak is in perfect agreement with the pre-edge peak position of the CoO reference spectrum, while the second peak is shifted by approximately 3 eV relative to XANES of metallic cobalt which is due to Co-N as observed for cobalt phthalocyanine encapsulated in multi-walled carbon nanotubes.[22] Above the absorption edge, there are two peaks of relatively low intensity at 7725 and 7732 eV ("b" and "c" in Figure 4a). Both energies coincide with distinctive features of CoO and cobalt foil. The lower energy peak is, however, considerably more intense than the one for Co foil and therefore formed by overlapping patterns of both references used.

In the extended X-ray fine structure (EXAFS, Figure 4b), there are indications of both light backscattered and cobalt being present in the first coordination sphere. The low distance peak at $r = 1.4$ Å is presumably formed by both Co–O and Co–N backscattering events. Although the presence of nitrogen in the first coordination sphere is not clearly

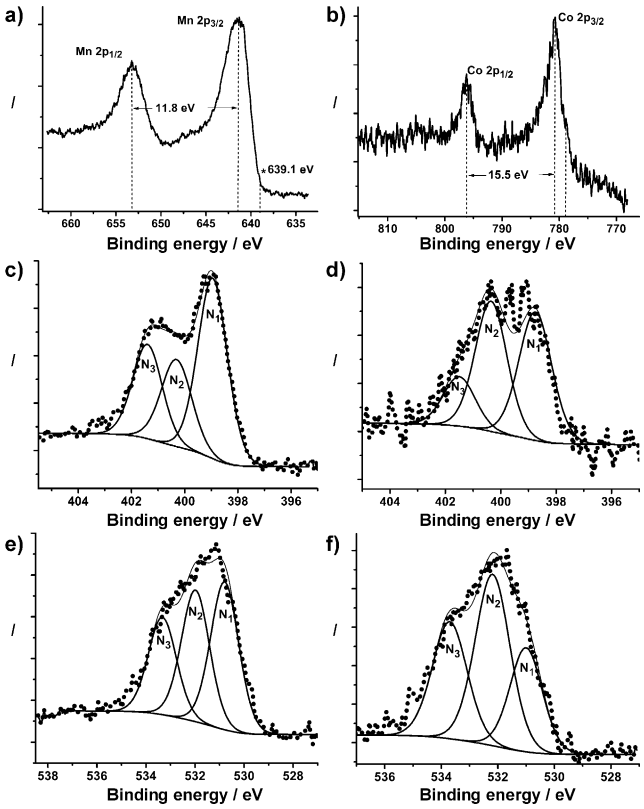

Figure 3. XPS spectra showing the 2p core-level spectra of Mn in Mn_xO_y/NC (a) and Co in Co_xO_y/NC (b), N 1s spectra of Mn_xO_y/NC (c) and Co_xO_y/NC (d), and high-resolution O1s spectra of oxygen in Mn_xO_y/NC (e) and in Co_xO_y/NC (f).

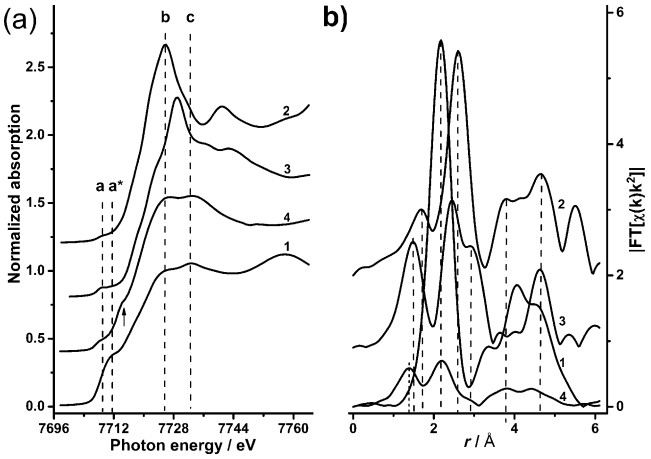

Figure 4. a) XANES, and b) EXAFS spectra of Co_xO_y/NC (4) and references Co foil (1), CoO (2), and Co_3O_4 (3). The shoulder at about 7714.1 eV (see arrow) confirms intimate interaction between Co and N and thus the existence of Co–N_x moieties.

evident, it can be distinguished by the broader and lower peak intensity indicating the interference of two waves with almost equal period, but shifted in phase to form a not perfectly favorable interference pattern (see Figure 8S).

Fitting of the EXAFS spectrum in the *k*-space shows that the local environment of Co can be better described by a three-shell model including Co–O, Co–N, and Co–Co scattering events (goodness of fit $R = 9.6\,\%$) rather than the two-shell model which includes only oxygen and cobalt as first-coordination-shell neighbors (goodness of fit $R = 14.5\,\%$). The corresponding fit parameters are provided in Table 2.

These observations lead us to conclude that during the pyrolysis step, the complexes degrade but the MN_4 core of the metallomacrocyclic ring is largely conserved (Scheme 1), and, the metallic species in B undergo oxidation to form metal oxides or surface oxide species during the calcination step. Structure B(I) is a known active site for ORR and is obtained by pyrolysis of N_4-macrocyclic complexes $< 700\,°C$, particularly those containing Fe and Co.[18,23] Structures C(II) and C(IV) are variants of B(I) and B(II), respectively, and are expected to be thermodynamically more stable than their B counterparts, since their formation results in saturation of the coordination capacity of the metals. We suppose that the unique simultaneous and interactive presence of nitrogen functionalized carbon groups, Mn–N_x and Co–N_x moieties, and the spinels of the respective metals are responsible for the remarkable capability of Mn_xO_y/NC and Co_xO_y/NC to catalyze both ORR and OER with such exceptional efficiency.

In particular, the nitrogen-doped carbon surrounding the metal oxide nanoparticles concertedly enhances the electrocatalytic performance of the oxides by improving their conductivity and complementarily catalyzing the ORR. The long-term performance of the catalysts was evaluated using double-pulse chronopotentiometry, with each pulse lasting one hour and alternating between oxygen evolution and oxygen reduction (Figure 9S). The catalysts last a few cycles then rapidly degrade owing to physical detachment of the catalyst films caused by the gas-bubble effect. Generally, Mn_xO_y/NC was the least stable, while Co_xO_y/NC and Ni_xO_y/NC had similar stability, maintaining a fairly constant overvoltage between oxygen reduction and oxygen evolution before degradation occurred.

In conclusion we uncovered a method for synthesis of inexpensive catalysts for bifunctional oxygen electrodes with potential application in metal–air batteries, unitized regenerative fuel cells, and alkaline electrolyzers. Mn_xO_y/NC and Co_xO_y/NC showed much lower overvoltage between the OER and ORR reactions compared to the state-of-the art catalysts RuO_2, IrO_2 and Pt/C (Pt (20 %) on carbon), which places them among the best bifunctional catalysts for oxygen electrodes reported to date.

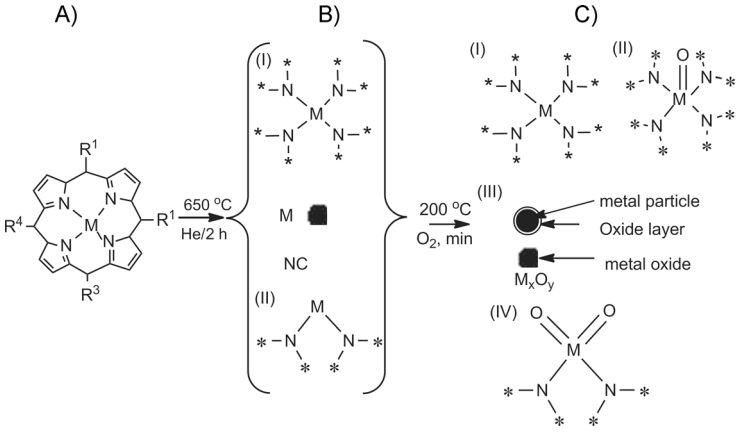

Scheme 1. Schematic illustration of the possible groups that are formed during pyrolysis of cobalt and manganese N_4-metallomacrocyclic complexes at 650 °C for 2 h under He, and subsequent calcination in oxygen at 200 °C for 30 min.

Table 2: Co*K*-edge EXAFS fitting using 3- and 2-shell models.[a]

	r [Å]	CN	*R* [%]
3-shell model			
Co-O	1.99	2.31	9.6
Co-N	1.88	1.45	
Co-Co	2.52	2.04	
2-shell model			
Co-O	1.90 ± 0.02	3.57 ± 0.42	14.5
Co-Co	2.54 ± 0.01	1.92 ± 0.32	

[a] *r* = distance from the central Co to the backscattering atom, CN = apparent coordination number, *R*-factor, indicating goodness of fit.

Received: February 22, 2014
Published online: June 27, 2014

Keywords: heterogeneous catalysts · nanoparticles · nitrogen-doped carbon · oxygen reduction · water oxidation

[1] G. Girishkumar, B. McCloskey, A. C. Luntz, S. Swanson, W. Wilcke, *J. Phys. Chem. Lett.* **2010**, *1*, 2193 – 2203.
[2] a) K. M. Abraham, *J. Electrochem. Soc.* **1996**, *143*, 1; b) S. W. Lee, C. Carlton, M. Risch, Y. Surendranath, S. Chen, S. Furutsuki, A. Yamada, D. G. Nocera, Y. Shao-Horn, *J. Am. Chem. Soc.* **2012**, *134*, 16959 – 16962.
[3] J.-S. Lee, S. T. Kim, R. Cao, N.-S. Choi, M. Liu, K. T. Lee, J. Cho, *Adv. Energy Mater.* **2011**, *1*, 34 – 50.
[4] J. Christensen, P. Albertus, R. S. Sanchez-Carrera, T. Lohmann, B. Kozinsky, R. Liedtke, J. Ahmed, A. Kojic, *J. Electrochem. Soc.* **2012**, *159*, R1.
[5] a) V. Nikolova, P. Iliev, K. Petrov, T. Vitanov, E. Zhecheva, R. Stoyanova, I. Valov, D. Stoychev, *J. Power Sources* **2008**, *185*, 727 – 733; b) G. Chen, S. R. Bare, T. E. Mallouk, *J. Electrochem. Soc.* **2002**, *149*, A1092; c) Y. Shao, S. Park, J. Xiao, J.-G. Zhang, Y. Wang, J. Liu, *ACS Catal.* **2012**, *2*, 844 – 857.
[6] T. Reier, M. Oezaslan, P. Strasser, *ACS Catal.* **2012**, *2*, 1765 – 1772.
[7] I. Katsounaros, S. Cherevko, A. R. Zeradjanin, K. J. J. Mayrhofer, *Angew. Chem.* **2014**, *126*, 104 – 124; *Angew. Chem. Int. Ed.* **2014**, *53*, 102 – 121.
[8] L. Jörissen, *J. Power Sources* **2006**, *155*, 23 – 32.
[9] F.-D. Kong, S. Zhang, G.-P. Yin, Z.-B. Wang, C.-Y. Du, G.-Y. Chen, N. Zhang, *Int. J. Hydrogen Energy* **2012**, *37*, 59 – 67.
[10] F. Cheng, J. Shen, B. Peng, Y. Pan, Z. Tao, J. Chen, *Nat. Chem.* **2011**, *3*, 79 – 84.
[11] a) Y. Liang, Y. Li, H. Wang, J. Zhou, J. Wang, T. Regier, H. Dai, *Nat. Mater.* **2011**, *10*, 780 – 786; b) Z. Jian, P. Liu, F. Li, P. He, X. Guo, M. Chen, H. Zhou, *Angew. Chem.* **2014**, *126*, 452 – 456; *Angew. Chem. Int. Ed.* **2014**, *53*, 442 – 446.
[12] F. Buciuman, F. Patcas, R. Craciun, D. R. T. Zahn, *Phys. Chem. Chem. Phys.* **1999**, *1*, 185 – 190.
[13] R. R. Gaughan, D. F. Shriver, L. J. Boucher, *Proc. Natl. Acad. Sci. USA* **1975**, *72*, 433 – 436.
[14] Y. Gorlin, T. F. Jaramillo, *J. Am. Chem. Soc.* **2010**, *132*, 13612 – 13614.
[15] J. W. Lee, A. S. Hall, J.-D. Kim, T. E. Mallouk, *Chem. Mater.* **2012**, *24*, 1158 – 1164.
[16] M. C. Biesinger, B. P. Payne, A. P. Grosvenor, L. W. Lau, A. R. Gerson, R. S. Smart, *Appl. Surf. Sci.* **2011**, *257*, 2717 – 2730.
[17] T. Okada, M. Gokita, M. Yuasa, I. Sekine, *J. Electrochem. Soc.* **1998**, *145*, 815 – 822.
[18] M. Ladouceur, *J. Electrochem. Soc.* **1993**, *140*, 1974 – 1981.
[19] C. V. Rao, C. R. Cabrera, Y. Ishikawa, *J. Phys. Chem. Lett.* **2010**, *1*, 2622 – 2627.
[20] S. Kundu, W. Xia, W. Busser, M. Becker, D. A. Schmidt, M. Havenith, M. Muhler, *Phys. Chem. Chem. Phys.* **2010**, *12*, 4351 – 4359.
[21] S. C. Petitto, E. M. Marsh, G. A. Carson, M. A. Langell, *J. Mol. Catal. A* **2008**, *281*, 49 – 58.
[22] J. C. Swarbrick, T.-C. Weng, K. Schulte, A. N. Khlobystov, P. Glatzel, *Phys. Chem. Chem. Phys.* **2010**, *12*, 9693 – 9699.
[23] a) G. Faubert, G. Lalande, R. Cote, D. Guay, J. P. Dodelet, L. T. Weng, P. Bertrand, G. Denes, *Electrochim. Acta* **1996**, *41*, 1689 – 1701; b) Z. Shi, H. Liu, K. Lee, E. Dy, J. Chlistunoff, M. Blair, P. Zelenay, J. Zhang, Z.-S. Liu, *J. Phys. Chem. C* **2011**, *115*, 16672 – 16680; c) M. Yuasa, A. Yamaguchi, H. Itsuki, K. Tanaka, M. Yamamoto, K. Oyaizu, *Chem. Mater.* **2005**, *17*, 4278 – 4281; d) J. Masa, A. Zhao, W. Xia, M. Muhler, W. Schuhmann, *Electrochim. Acta* **2014**, *128*, 271 – 278.

